small methods
www.small-methods.com

Probing the Local Electronic Structure in Metal Halide Perovskites through Cobalt Substitution

Amir A. Haghighirad, Matthew T. Klug, Liam Duffy, Junjie Liu, Arzhang Ardavan, Gerrit van der Laan, Thorsten Hesjedal, and Henry J. Snaith*

Owing to the unique chemical and electronic properties arising from 3d-electrons, substitution with transition metal ions is one of the key routes for engineering new functionalities into materials. While this approach has been used extensively in complex metal oxide perovskites, metal halide perovskites have largely resisted facile isovalent substitution. In this work, it is demonstrated that the substitution of Co^{2+} into the lattice of methylammonium lead triiodide imparts magnetic behavior to the material while maintaining photovoltaic performance at low concentrations. In addition to comprehensively characterizing its magnetic properties, the Co^{2+} ions themselves are utilized as probes to sense the local electronic environment of Pb in the perovskite, thereby revealing the nature of their incorporation into the material. A comprehensive understanding of the effect of transition metal incorporation is provided, thereby opening the substitution gateway for developing novel functional perovskite materials and devices for future technologies.

1. Introduction

The promise of low-cost and efficient optoelectronic devices has been the central driving force behind the recent development of metal halide perovskite materials.[1–3] While this effort has achieved single-junction photovoltaic devices reaching 25.7% certified power conversion efficiencies and light-emitting diodes with external quantum efficiencies exceeding 20%,[4–6] the demonstrated functionality of metal halide perovskites is substantially limited when compared with their metal oxide perovskite counterparts, which display a wide range of physical properties such as ferroelectricity,[7] piezoelectricity,[8] photocatalysis,[9] superconductivity,[10] and colossal magnetoresistance.[11] Materials research and development efforts to date have focused almost exclusively on understanding and improving the underlying optoelectronic properties of metal halide perovskites with substantially fewer reports probing additional properties such as magnetism,[12,13] piezoelectricity,[14,15,8] and photocatalysis.[16–18] The restricted functionality of 3D halide perovskites versus their oxide analogs is largely due to the limited number of metal ions that have proven capable of occupying the B-site of the ABX_3 lattice. With regards to photovoltaic performance, the most successful metal species to date is Pb^{2+}, with Sn^{2+} being a far second owing to its instability against oxidation.[19] While double perovskites that preserve charge neutrality by blending a trivalent and monovalent ion in equal parts have been formed,[20–23] and modest photovoltaic performance has recently been demonstrated,[24,25] this subclass of metal halide materials tends to display indirect bandgaps,[20–22] reduced charge carrier transport properties, or intrinsic chemical instability that limit their usefulness. Instead of full Pb substitution, a promising pathway to generating perovskite materials with new metal compositions is through partial B-site replacement.[26] However, success with this approach has also been limited since extrinsic metal ions tend to either become excluded from the perovskite lattice and segregate elsewhere (e.g., Al^{3+}, Sr^{2+}, Fe^{2+}),[27,28] or appear to incorporate into the lattice but introduce defect states that detrimentally impact optoelectronic quality when more than a few molar percent of Pb^{2+} is replaced (e.g., Mn^{2+}, Co^{2+}).[27,29,30] Transition metal ions are of particular interest for incorporation into mixed-metal halide perovskites because their electronic configurations offer the opportunity to introduce new functionality into the material.[29,31,32] Although reports remain relatively limited, it has been demonstrated that Mn^{2+} incorporates into

A. A. Haghighirad, M. T. Klug, L. Duffy, J. Liu, A. Ardavan, T. Hesjedal, H. J. Snaith
Department of Physics
University of Oxford
Clarendon Laboratory
Oxford OX1 3PU, UK
E-mail: thorsten.hesjedal@physics.ox.ac.uk
A. A. Haghighirad
Institute for Quantum Materials and Technologies
Karlsruhe Institute of Technology
76021 Karlsruhe, Germany
G. van der Laan
Diamond Light Source
Harwell Science and Innovation Campus
Didcot OX11 0DE, UK

The ORCID identification number(s) for the author(s) of this article can be found under https://doi.org/10.1002/smtd.202300095

DOI: 10.1002/smtd.202300095

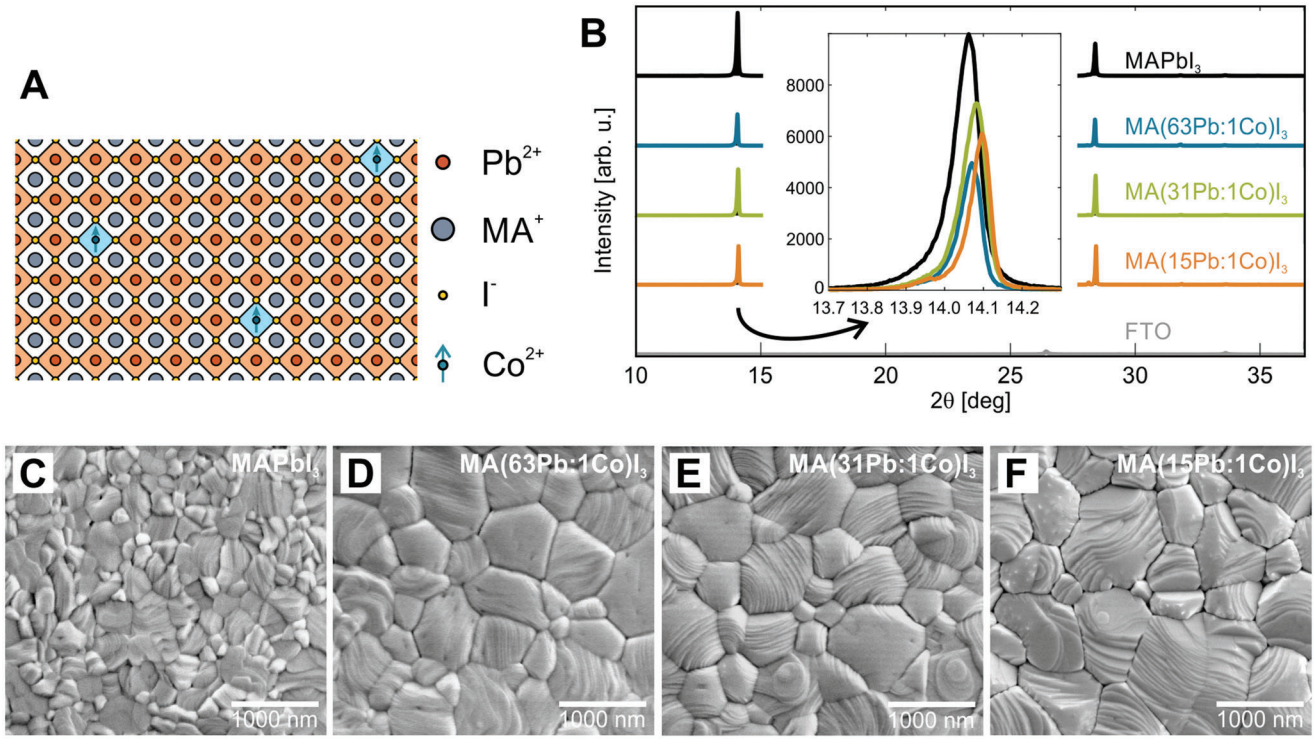

Figure 1. Structural properties of the magnetic perovskite semiconductor MA(Pb:Co)I_3. A) Illustration of Co^{2+} ions partially occupying the B-sites of the $MAPbI_3$ host material. B) X-ray diffraction spectra of MA(Pb:Co)I_3 films prepared using the gas quenching method on FTO substrate (see Supporting Information for details). The close-up shows the first peak shifting to larger diffraction angles with increasing Co concentration. Scanning electron micrographs of C) $MAPbI_3$, D–F) MA(Pb:Co)I_3 films produced through gas quenching. For the Co-substituted samples, the morphology and the grain size are comparable.

cesium lead halide nanocrystals and produces subgap luminescence through a d–d transition of the extrinsic ions,[33–36] whereas single crystals of $MAPb_{0.9}Mn_{0.1}I_3$ have demonstrated magnetic behavior,[12] and Ruddlesden-Popper halide perovskite display magnetically brightened excitonic luminescence upon Mn^{2+} doping.[37] Crystallographic evidence that Co^{2+} is capable of partially replacing Pb^{2+} at the B-site of $MAPbI_3$, presenting a means to modify the energetics of the perovskite material without changing the bandgap or reducing the power conversion efficiency in p–i–n solar cells upon substitution,[38] was limited to a few percent.[29,31] This observation has been questioned by the finding of Kubicki et al.,[39] who provide evidence based on solid-state NMR that Co^{2+} is not capable of substitutionally doping $MAPbI_3$ but rather concludes it clusters into an impurity phase.

Here, we experimentally demonstrate that Co^{2+} ions are incorporated into the bulk perovskite crystal structure. We use Co^{2+} ions themselves to sense the local electronic environment of Pb by performing a study of the magnetic properties of the system by electron spin resonance (ESR), superconducting quantum interference device (SQUID) magnetometry, and X-ray magnetic circular dichroism (XMCD) using synchrotron radiation. These techniques reveal that Co^{2+} ions possess a high-spin configuration in an octahedral crystal field, imparting paramagnetic behavior to the perovskite thin film material.

2. Results and Discussion

2.1. Sample Growth and Halide Substitution

Alloyed perovskites are formed by substitution on A, B, and X sites in the ABX_3 perovskite structure, where A is a 1+ cation (typically methylammonium (MA), formamidinium (FA), or cesium (Cs^+)), B is a metal cation such as lead (Pb^{2+}) or tin (Sn^{2+}), and X is a halide anion (Cl^-, Br^- or I^-) (**Figure 1**A). Directing the final composition of a compound metal halide perovskite films, where multiple ions are located at a particular site of the ABX_3 lattice, is often not straightforwardly determined by the precursor stoichiometry. Local compositional heterogeneity has been identified in both mixed A-site systems [40] and mixed X-site systems,[41] and photoinduced halide segregation at the X-site is a well-known phenomenon that occurs in certain mixed-halide compositions.[42–44] Likewise, in the most common example of a mixed-metal system, where Pb and Sn are alloyed to narrow the bandgap down to ≈1.24 eV, there is evidence that the metal species are not homogeneously distributed throughout the film.[38,45] It has been reported that upon simply dissolving the halide precursor materials in standard solvents, such as dimethylformamide or dimethylsulfoxide, the ions do not fully dissociate but rather remain loosely networked forming soft colloids that help template the perovskite during thin-film formation.[46–49]

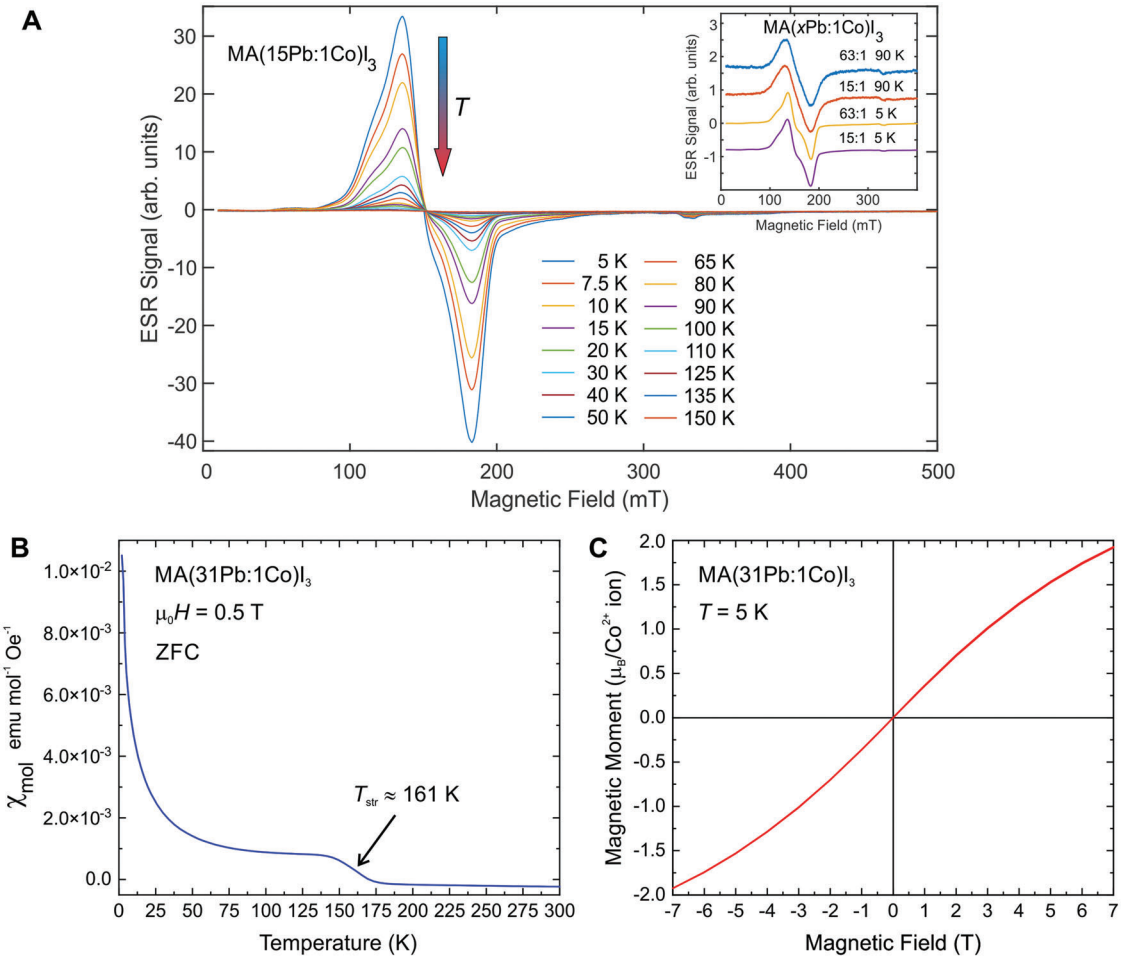

Figure 2. Magnetic properties of MA(Pb:Co)I_3 samples for different Co concentrations. A) ESR spectra for a range of temperatures from 5 to 150 K for a MA(15Pb:1Co)I_3 sample. The signal gradually reduces for higher temperature *T*. Inset: Comparison of the line shapes of the Pb:Co = 63:1 and 15:1 sample at 1.5 and 90 K. The spectra are scaled and offset for better comparison. B) Magnetic susceptibility versus temperature plot obtained after zero-field cooling (ZFC), and measured during warming up in an applied field of 0.5 T. The structural transition from tetragonal to orthorhombic reveals itself by a small step at $T_{str} \approx 161$ K. C) Magnetization versus field (hysteresis) plot at a temperature of 5 K for MA(31Pb:1Co)I_3.

To promote the mixing of the Co and Pb ions at the B-site, lead(II) iodide and cobalt(II) iodide underwent a high-temperature solid-state reaction to form an alloyed material with molar metal ratios of Pb:Co = {63:1, 31:1, and 15:1}. The alloyed iodide material was then further reacted stoichiometrically with methylammonium iodide in the solid state to form the mixed-metal perovskite material. Thin films were cast by spin-coating ink prepared from the perovskite powders. Powder X-ray diffraction (Figure 1B and Figure S3, Supporting Information) of the resultant films do not show any evidence of impurity phases such as PbI_2, CoI_2, or MA_2CoI_4,[50] but rather show perovskite diffraction peaks that shift to higher diffraction angles with increasing Co concentration. This finding is in agreement with our previous report [29] and consistent with the smaller sized Co ion becoming incorporated at the B-site of the perovskite lattice, and in contrast to the finding of Kubicki et al.,[39] who show that Co^{2+} is not capable of substitutionally doping $MAPbI_3$. Details of the sample preparation and characterization can be found in the Supporting Information. As shown in Figure 1C–F, this approach produces pinhole-free perovskite films.

2.2. Electron Spin Resonance

Variable-temperature electron spin resonance (ESR) measurements were performed on two powder samples with different Co concentrations (Pb:Co = 63:1 and 15:1). The representative (normalized) ESR spectra are shown in **Figure 2**A. In contrast to the report by Kubicki et al.[39] where ESR spectra were not detected, we observe clear ESR resonances that appear independent of the substitution level, which suggests that the Co atoms are homogeneously incorporated into the host material and that no concentration-dependent Co clustering is present. At high temperatures, a single ESR resonance feature is observed in both samples with an effective *g*-value, $g_{eff} = 4.36$, which is in good agreement with the experimental literature values for Co^{2+} in the octahedral environment.[51] Upon decreasing the temperature, additional fine features start to emerge as shoulders, while the overall width and center of the ESR resonance remain fixed and are temperature independent. The emergence of the additional features is likely due to the tetragonal to orthorhombic structural transition, as well as the freezing out of the lattice

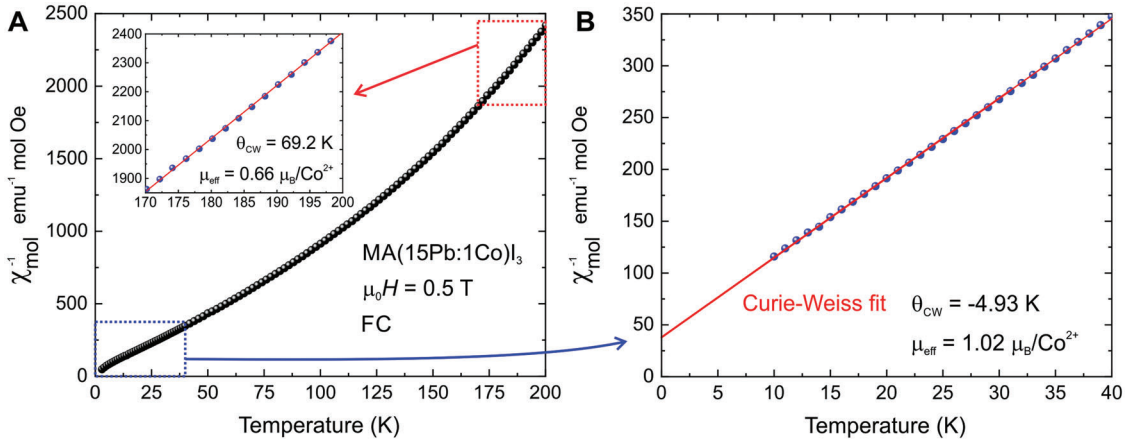

Figure 3. Curie-Weiss behavior of MA(Pb:Co)I_3 thin films. A) Inverse susceptibility versus temperature for MA(15Pb:1Co)I_3 measured after field-cooling (FC). The inset shows the Curie-Weiss behavior of the susceptibility above 170 K (indicated by red rectangle). B) Inverse susceptibility versus temperature with a Curie-Weiss fit in the temperature range 10–40 K (indicated by blue rectangle in (A)).

vibrations. At low temperatures, the octahedral environment of the Co atoms is distorted, leading to a small anisotropy, i.e., anisotropic g_{eff} values and/or zero-field splitting, which appear as unresolved fine structures in the 5 K ESR spectrum. Since the width as well as the position of the resonance appear to be insensitive to the temperature, the magnetic interactions between the Co spins are expected to be weak down to the lowest reachable temperature (5 K).

2.3. SQUID Magnetometry

In order to characterize the effect of Co substitution on the magnetic properties of MA(Pb:Co)I_3, we measured the susceptibility $X_{mol}(T)$ and the isothermal magnetic hysteresis loops $M(H)$ for the selected samples with nominal Co molar concentrations of 1.6, 3.1, and 6.2%. The magnetic measurements were performed using a superconducting quantum interference device (SQUID) magnetometer in fields of up to 7 T and the results are shown in Figure 2B,C, and in the Supporting Information.

The magnetic susceptibility curves, $X_{mol}(T)$, for all concentrations show that the magnetization increases significantly with decreasing temperature, which is an indication for paramagnetic behavior. Figure 2C and Figure S12 (Supporting Information) display the isothermal magnetization at 3 and 5 K for Co concentrations of 1.6 and 6.3%, respectively. The temperatures are fixed at 3 and 5 K. For all Co substitutions, the hysteresis loops are hardly observable down to 3 K, while the saturation tendency persists (see Figures S11 and S12, Supporting Information). A small ferromagnetic contribution superimposed on an overall paramagnetic state cannot be excluded. One could anticipate the Co sublattice being paramagnetic while an additional ferromagnetic component is present, presumably from defects in the lattice (see XMCD section below). There is some indication of superparamagnetism in the M–H curves for 1.6% Co (see Figure S11, Supporting Information).

The temperature dependence of the dc magnetic susceptibility is shown in **Figure 3** and Figures S11a and S12a (Supporting Information). In the high-temperature range, the susceptibility increases linearly for Co concentrations of 1.6, 3.1. and 6.3% with decreasing temperature down to 160 K, following a Curie-Weiss behavior.

There is a change of slope in the inverse susceptibility $X^{-1}(T)$ below ≈165 K, which is due to a well-known structural transition from tetragonal to orthorhombic (see Figure 3). Note that we observe no magnetic transitions at lower temperatures, which could be linked to impurities, such as CoI_2, which has a Néel temperature of 11 K and a first-order transition at 9.4 K.[52]

Figure 3A presents the temperature dependence of the inverse magnetic susceptibility $X^{-1}(T)$. In the inset, the Curie-Weiss behavior of susceptibility above 170 K for MA(15Pb:1Co)I_3 is shown. The data fit well to $X(T) = \frac{C}{T-\theta_{CW}} + X_0$, where C is the Curie constant, θ_{CW} is the paramagnetic Curie temperature, and X_0 is a temperature-independent constant to account for the diamagnetic contribution. The M–H magnetization curves for different Co substitution levels are shown in Figure 3A and Figures S11a and S12a (Supporting Information). The maximum magnetization corresponds to a magnetic moment of ≈0.66 μ_B/Co^{2+} at a field of 2 T (Figure 2C). This agrees reasonably well with the value obtained from the XMCD sum rules (which is discussed in detail in Section 2.4 below), which is $(m_L + m_S) = 0.52$ μ_B/Co^{2+} at 3 K and a field of 2 T. Due to competing antiferromagnetic and superexchange interactions between neighboring Co ions, only a fraction of the Co^{2+} ions are expected to order ferromagnetically at 2 T. In these films, the magnetization is far from saturation. The moment of high-spin Co^{2+} ($3d^7$) in octahedral crystal field ($10Dq = 0.7$ eV) is ≈2.2 μ_B, while that of metallic Co is ≈1.8 μ_B. The exchange coupling between Co–Co nearest neighbors in $MAPbI_3$ hints to an antiferromagnetic interaction being dominant at low temperatures (see Figure 3B). A likely scenario for the observation of a reduced moment in the films at low temperatures is the competition of different magnetic ordering mechanisms, such as Co-defect pair ferromagnetism, Co–Co antiferromagnetic exchange, and isolated paramagnetic Co ions. While we are not able to unravel the detailed mechanism with the data at hand, it is clear that for large Co concentrations, there will be more Co defect pairs present which can reduce the effective moment per Co atom.

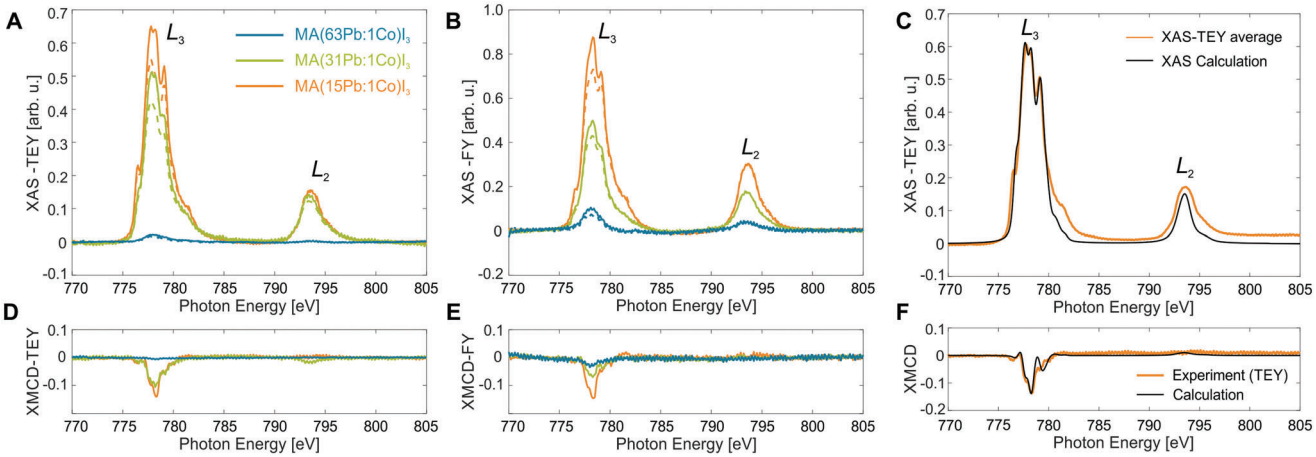

Figure 4. Magnetic X-ray spectroscopy on MA(Pb:Co)I_3 films. Co $L_{2,3}$ XAS and XMCD spectra of MA(Pb:Co)I_3 films measured at 3 K in an applied magnetic field of 2 T. XAS signals for right- (solid lines) and left-circularly polarized (dashed lines) as measured by A) total-electron yield (TEY) and B) fluorescence yield (FY). Corresponding XMCD signals as obtained from the difference between the two circular polarization measurements of D) TEY and E) FY. Comparison of measured and calculated C) averaged XAS and F) XMCD TEY spectra of the Co:MAPbI_3 sample grown on MgO with medium Co concentration, i.e., 15Pb:1Co. The calculated results are shown for the high-spin Co d^7 configuration in an octahedral crystal field. In order to facilitate the comparison between the line shapes, the calculated XAS is normalized to the experiment, whilst the corresponding calculated XMCD is scaled down by a factor 0.09.

2.4. X-Ray Magnetic Circular Dichroism

To unambiguously identify that Co ions are responsible for the magnetic properties observed with ESR and SQUID, X-ray absorption spectra (XAS) at the Co $L_{2,3}$ edges of MA(Pb:Co)I_3 films were measured using synchrotron radiation on beamline I10 at the Diamond Light Source. The XAS measurements were made in surface-sensitive total-electron yield (TEY) mode and bulk-sensitive fluorescence yield (FY) mode.[53]

The Co $L_{2,3}$ edges are clearly observed in all samples, with the FY mode demonstrating signal intensities that are nearly linear with Co concentration. The element-specific XMCD technique is able to probe the local electronic character of the magnetic ground state.[54] The XMCD signal is obtained by taking the difference between two XAS spectra recorded with the X-ray helicity vector and applied magnetic field parallel and antiparallel, respectively. The measurements were performed by reversing the polarization of the incident X-rays. A field of 2 T was applied during the measurements with the field along the X-ray beam at an incident angle of 30° relative to the surface normal. During the change between different temperatures, and for the initial cool down, no magnetic field was applied. The XAS and XMCD results are shown in **Figure 4**a,b for the measurements at a temperature of 3 K in TEY and FY mode, respectively.

2.5. XMCD Analysis and Multiplet Calculations

Figure 4C,F shows a comparison of the XAS and XMCD spectra obtained from measurements and multiplet calculations (details on the multiplet calculations are given in the Supporting Information). A satisfactory agreement is achieved for Co having a high-spin d^7 configuration in an octahedral (O_h) crystal field. The ground state is a spin quintet $t_{2g}^5 e_g^2$ ($^4T_{1g}$) state, which is split by first-order spin-orbit interaction into four levels, of which only the lowest level (*E*′) is significantly Boltzmann occupied.

From the sum rule analysis,[53] the orbital and spin moments, as well as the averaged spectroscopic splitting factor (*g*-factor) are obtained as $m_L = 0.2075\ \mu_B$/Co, $m_S = 0.311\ \mu_B$/Co, and $g_{av} = 3.33$ (details of the analysis can be found in the Supporting Information). On the other hand, the calculated spectrum gives $m_L = 0.652\ \mu_B$/Co, $m_S = 1.54\ \mu_B$/Co, and $g_{av} = 2.85$, i.e., a large difference in m_L/m_S and hence *g* is observed. This can be partly ascribed to the challenge correcting for the cumbersome background in the experimental XMCD data. Also, a small distortion of the octahedral site symmetry—not accounted for in the calculation—can modify the orbital moment. Note that observed spin and orbital moments which are 11% of the calculated crystal field values for Co^{2+} are relatively small.

By performing a study of the magnetic properties of MA(Pb:Co)I_3 by ESR, SQUID magnetometry, and XAS/XMCD, we were able to reveal that Co^{2+} ions possess a high-spin configuration in an octahedral crystal field, imparting paramagnetic behavior to the perovskite thin film material. This finding is in contrast to the work by Kubicki et al.,[39] who show that Co^{2+} is not capable of substitutionally doping MAPbI_3.

2.6. Photovoltaic Performance

Finally, we investigated the effects of Co substitution on the bandgap and the performance of the solar cells for the different Co concentrations using the procedure detailed in the Supporting Information.

The current–voltage (*J*–*V*) curves for the optimized solar cells are shown in **Figure 5**A. The steady-state power conversion efficiency (PCE) for these optimized cells reduces from 16.14% for MAPbI_3 to 8.29% for MA(15Pb:1Co)I_3 (Figure 5B), which is an effect of the Co^{2+}, which can act as centers for non-radiative recombination, affecting the PL lifetime in complex ways (see Figure S7, Supporting Information), as has been discussed in detail in ref. [#0029]. Note that the *J*–*V* curves are increasingly

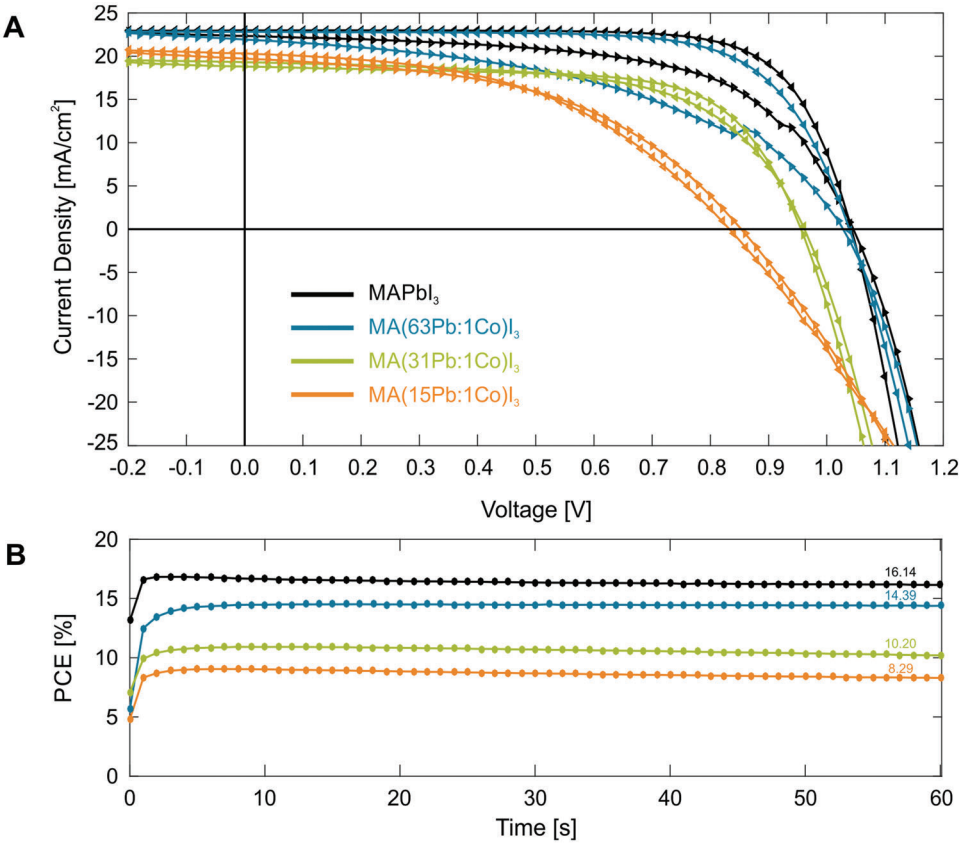

Figure 5. A) Current–voltage characteristics for forward (triangles pointing to the right) and backward (triangles pointing to the left) biased measurements for MA(Pb:Co)I_3. B) Stabilized power output (power conversion efficiency, PCE) of the champion MA(Pb:Co)I_3 solar cells as a function of time.

becoming nonhysteretic with Co incorporation, which is due to unbalanced charge carrier transport due to doping, and variation of the charge trap density due changes in morphology (compare Figure 1C–F).[55]

The measurements of the external quantum efficiency were performed using a custom-built Fourier transform photocurrent spectroscopy system, and by plotting the data against the photon energy, the bandgap energy E_g is obtained, showing a fixed value of 1.58 V and no dependence on the Co concentration (Figure S4, Supporting Information), which is also consistent with our previous work. The ability of these mixed-metal films to function as efficient solar cells, while also presenting magnetic properties in thin films, leads us to conclude that the MA(Pb:Co)I_3 perovskites constitute a new class of paramagnetic semiconductors.

3. Conclusion

In conclusion, we have explored isovalent substitution of Pb^{2+} with Co^{2+} ions in $MAPbI_3$ perovskite films. Cobalt serves as a paramagnetic probe that enables the systematic exploration of doping and alloying of this important materials class by probing the electronic environment of Pb. Using magnetometry, ESR and XAS/XMCD, we found that in $MAPb_{1-x}Co_xI_3$, Co^{2+} is in an octahedral environment with a high-spin $t_{2g}^5e_g^2$ configuration. The photovoltaic performance of the Co-doped $MAPbI_3$ films was measured and only a moderate reduction of their photovoltaic performance and photoluminescence was found for low Co concentrations, while the bandgap remained unaffected. With the demonstration that doping with Co^{2+} leads to magnetic bulk behavior, this material is the first multifunctional mixed-metal halide perovskite system that exhibit both paramagnetic properties and efficient photovoltaic performance. By demonstrating that the Co^{2+} ions themselves can act as probes to sense the local crystal field in perovskite thin films, we open the opportunity to similarly characterize the crystallographic environment of other Co-doped 2D and 3D perovskite systems and rationally design them to display new and tunable functionalities.

4. Experimental Section

A detailed discussion of the synthesis, the material and the photovoltaic characterization methods can be found in the Supporting Information.

Statistical Analysis: (1) Pre-processing: The data presented in Figure 4 was averaged over six scans (three with left and three with right circularly polarized light). (2) Mean values and standard deviations are not relevant for the presented figures. (3) The number of data points in the XRD spectra is typically 1000 (Figure 1B), in the ESR spectra (Figure 2A) 5000 for every temperature, in the magnetic hysteresis curve (Figure 2C) 200 field points, and in the XAS/XMCD spectra (Figure 4) 351 energy points (covering the range from 770 to 805 eV in steps of 0.1 eV). (4) No statistical methods were employed to test the hypotheses in this work. (5) The magnetic parameters, extracted from fitting the (linear) Curie-Weiss law to the inverse susceptibility (Figure 3B), were obtained using Origin.

Supporting Information

Supporting Information is available from the Wiley Online Library or from the author.

Acknowledgements

A.A.H. and M.T.K. contributed equally to this work. Financial support from the Engineering and Physical Sciences Research Council (EPSRC) under award numbers EP/M020517/1, EP/P000479/1, and EP/M005143/1 are gratefully acknowledged. L.D. acknowledges studentship support from EPSRC and the Science and Technology Facilities Council (UK). The authors thank the Diamond Light Source for provision of beamtime (SI-16141).

Conflict of Interest

H.J.S. is a co-founder and Chief Science Officer of Oxford PV, which is commercializing perovskite-based photovoltaics.

Data Availability Statement

The data that support the findings of this study are available from the corresponding author upon reasonable request.

Keywords

electron spin resonance, metal halide perovskites, optical spectroscopy, solar cells, X-ray magnetic spectroscopy

Received: January 28, 2023
Revised: February 14, 2023
Published online:

[1] A. Kojima, K. Teshima, Y. Shirai, T. Miyasaka, *J. Am. Chem. Soc.* **2009**, *131*, 6050.
[2] M. M. Lee, J. Teuscher, T. Miyasaka, T. N. Murakami, H. J. Snaith, *Science* **2012**, *338*, 643.
[3] C. C. Stoumpos, C. D. Malliakas, M. G. Kanatzidis, *Inorg. Chem.* **2013**, *52*, 9019.
[4] K. Lin, J. Xing, L. N. Quan, F. P. G De Arquer, X. Gong, J. Lu, L. Xie, W. Zhao, D. Zhang, C. Yan, W. Li, X. Liu, Y. Lu, J. Kirman, E. H. Sargent, Q. Xiong, Z. Wei, *Nature* **2018**, *562*, 245.
[5] B. Zhao, S. Bai, V. Kim, R. Lamboll, R. Shivanna, F. Auras, J. M. Richter, L. Yang, L. Dai, M. Alsari, X.-J. She, L. Liang, J. Zhang, S. Lilliu, P. Gao, H. J. Snaith, J. Wang, N. C. Greenham, R. H. Friend, D. Di, *Nat. Photonics* **2018**, *12*, 783.
[6] J. Cui, Y. Liu, Y. Deng, C. Lin, Z. Fang, C. Xiang, P. Bai, K. Du, X. Zuo, K. Wen, S. Gong, H. He, Z. Ye, Y. Gao, H. Tian, B. Zhao, J. Wang, Y. Jin, *Sci. Adv.* **2022**, *7*, eabg8458.
[7] S. Shahrokhi, W. Gao, Y. Wang, P. R. Anandan, Md Z Rahaman, S. Singh, D. Wang, C. Cazorla, G. Yuan, J.-M. Liu, T. Wu, *Small Methods* **2020**, *4*, 2000149.
[8] Y.-J. Kim, T.-V. Dang, H.-J. Choi, B.-J. Park, J.-H. Eom, H.-A. Song, D. Seol, Y. Kim, S.-H. Shin, J. Nah, S.-G. Yoon, *J. Mater. Chem. A* **2016**, *4*, 756.
[9] S. Park, W. J. Chang, C. W. Lee, S. Park, H.-Y. Ahn, K. T. Nam, *Nat. Energy* **2017**, *2*, 16185.
[10] D. B. Mitzi, C. A. Feild, W. T. A. Harrison, A. M. Guloy, *Nature* **1994**, *369*, 467.
[11] J. Wang, C. Zhang, H. Liu, R. Mclaughlin, Y. Zhai, S R. Vardeny, X. Liu, S. Mcgill, D. Semenov, H. Guo, R. Tsuchikawa, V. V. Deshpande, D. Sun, Z. V Vardeny, *Nat. Commun.* **2019**, *10*, 129.
[12] B. Náfrádi, P. Szirmai, M. Spina, H. Lee, O. V. Yazyev, A. Arakcheeva, D. Chernyshov, M. Gibert, L. Forró, E. Horváth, *Nat. Comm.* **2016**, *7*, 13406.
[13] T. Neumann, S. Feldmann, P. Moser, A. Delhomme, J. Zerhoch, T. Van De Goor, S. Wang, M. Dyksik, T. Winkler, J. J. Finley, P. Plochocka, M. S. Brandt, C. Faugeras, A. V. Stier, F. Deschler, *Nat. Commun.* **2021**, *12*, 3489.
[14] K.-Z. Du, Q. Tu, Xu Zhang, Q. Han, J. Liu, S. Zauscher, D. B. Mitzi, *Inorg. Chem.* **2017**, *56*, 9291.
[15] R. Pandey, G. Sb, S. Grover, S. K. Singh, A. Kadam, S. Ogale, U. V. Waghmare, V. R Rao, D. Kabra, *ACS Energy Lett.* **2019**, *4*, 1004.
[16] K. S. Schanze, P. V. Kamat, P. Yang, J. Bisquert, *ACS Energy Lett.* **2020**, *5*, 2602.
[17] J. Chen, C. Dong, H. Idriss, O. F. Mohammed, O. M. Bakr, *Adv. Energy Mater.* **2020**, *10*, 1902433.
[18] S. Park, S. Choi, S. Kim, K. T. Nam, *J. Phys. Chem. Lett.* **2021**, *12*, 8292.
[19] T. Leijtens, R. Prasanna, A. Gold-Parker, M. F. Toney, M. D. Mcgehee, *ACS Energy Lett.* **2017**, *2*, 2159.
[20] A. H. Slavney, T. Hu, A. M. Lindenberg, H. I. Karunadasa, *J. Am. Chem. Soc.* **2016**, *138*, 2138.
[21] E. T. Mcclure, M. R. Ball, W. Windl, P. M. Woodwardd, *Chem. Mater.* **2016**, *28*, 1348.
[22] G. Volonakis, M. R. Filip, A. A. Haghighirad, N. Sakai, B. Wenger, H. J. Snaith, F. Giustino, *J. Phys. Chem. Lett.* **2016**, *7*, 1254.
[23] F. Wei, Z. Deng, S. Sun, F. Xie, G. Kieslich, D. M. Evans, M. A. Carpenter, P. D. Bristowe, A. K. Cheetham, *Mater. Horiz.* **2016**, *3*, 328.
[24] W. Gao, C. Ran, J. Xi, B. Jiao, W. Zhang, M. Wu, X. Hou, Z. Wu, *ChemPhysChem* **2018**, *19*, 1696.
[25] M. Pantaler, K. T. Cho, V. I. E. Queloz, I. García Benito, C. Fettkenhauer, I. Anusca, M. K. Nazeeruddin, D. C. Lupascu, G. Grancini, *ACS Energy Lett.* **2018**, *3*, 1781.
[26] G. E. Eperon, D. S. Ginger, *ACS Energy Lett.* **2017**, *2*, 1190.
[27] Y. Zhou, J. Chen, O. M. Bakr, H.-T. Sun, *Chem. Mater.* **2018**, *30*, 6589.
[28] J. T.-W. Wang, Z. Wang, S. Pathak, W. Zhang, D. W. Dequilettes, F. Wisnivesky-Rocca-Rivarola, J. Huang, P. K. Nayak, J. B. Patel, H. A. Mohd Yusof, Y. Vaynzof, R. Zhu, I. Ramirez, J. Zhang, C. Ducati, C. Grovenor, M. B. Johnston, D. S. Ginger, R. J. Nicholas, H. J. Snaith, *J. Energy Environ. Sci.* **2016**, *9*, 2892.
[29] M. T. Klug, A. Osherov, A. A. Haghighirad, S. D. Stranks, P. R. Brown, S. Bai, J. T.-W. Wang, X. Dang, V. Bulović, H. J. Snaith, A. M. Belcher, *Energy Environ. Sci.* **2017**, *10*, 236.
[30] W. Liu, L. Chu, N. Liu, Y. Ma, R. Hu, Y. Weng, H. Li, J. Zhang, X'Ao Li, W. Huang, *J. Mater. Chem. C* **2019**, *7*, 11943.
[31] M. D. Sampson, J. S. Park, R. D. Schaller, M. K. Y. Chan, A. B. F. Martinson, *J. Mater. Chem. A* **2017**, *5*, 3578.
[32] B. Luo, F. Li, K. Xu, Y. Guo, Y. Liu, Z. Xia, J. Z. Zhang, *J. Mater. Chem. C* **2019**, *7*, 2781.
[33] W. Liu, Q. Lin, H. Li, K. Wu, I. Robel, J. M. Pietryga, V I. Klimov, *J. Am. Chem. Soc.* **2016**, *138*, 14954.
[34] D. Parobek, B. J. Roman, Y. Dong, H. Jin, E. Lee, M. Sheldon, D. H. Son, *Nano Lett.* **2016**, *16*, 7376.
[35] W. J. Mir, M. Jagadeeswararao, S. Das, A. Nag, *ACS Energy Lett.* **2017**, *2*, 537.
[36] H. Liu, Z. Wu, J. Shao, D. Yao, H. Gao, Y. Liu, W. Yu, H. Zhang, B. Yang, *ACS Nano* **2017**, *11*, 2239.
[37] A. Dutta, R. K. Behera, S. Deb, S. Baitalik, N. Pradhan, *J. Phys. Chem. Lett.* **2019**, *10*, 1954.
[38] A. R. Bowman, M. T. Klug, T. A. S. Doherty, M. D. Farrar, S. P. Senanayak, B. Wenger, G. Divitini, E. P. Booker, Z.

Andaji-Garmaroudi, S. Macpherson, E. Ruggeri, H. Sirringhaus, H. J. Snaith, S. D. Stranks, *ACS Energy Lett.* **2019**, *4*, 2301.
[39] D. J. Kubicki, D. Prochowicz, A. Pinon, G. Stevanato, A. Hofstetter, S. M. Zakeeruddin, M. Grätzel, L. Emsley, *J. Mater. Chem. A* **2019**, *7*, 2326.
[40] L. E. Mundt, F. Zhang, A. F. Palmstrom, J. Xu, R. Tirawat, L. L. Kelly, K. H. Stone, K. Zhu, J. J. Berry, M. F. Toney, L. T. Schelhas, *ACS Energy Lett.* **2022**, *7*, 471.
[41] K. Frohna, M. Anaya, S. Macpherson, J. Sung, T. A. S. Doherty, Y.-H. Chiang, A. J. Winchester, K. W. P. Orr, J. E. Parker, P. D. Quinn, K. M. Dani, A. Rao, S. D. Stranks, *Nat. Nanotechnol.* **2022**, *17*, 190.
[42] E. T. Hoke, D. J. Slotcavage, E. R. Dohner, A. R. Bowring, H. I. Karunadasa, M. D. Mcgehee, *Chem. Sci.* **2015**, *6*, 613.
[43] A. J. Knight, J. Borchert, R. D. J. Oliver, J. B. Patel, P G. Radaelli, H. J. Snaith, M. B. Johnston, L. M. Herz, *ACS Energy Lett.* **2021**, *6*, 799.
[44] S. G. Motti, J. B. Patel, R. D. J. Oliver, H. J. Snaith, M B. Johnston, L. M. Herz, *Nat. Commun.* **2021**, *12*, 6955.
[45] M. T. Klug, R. L. Milot, J. B. Patel, T. Green, H. C. Sansom, M. D. Farrar, A. J. Ramadan, S. Martani, Z. Wang, B. Wenger, J. M. Ball, L. Langshaw, A. Petrozza, M. B. Johnston, L. M. Herz, H. J. Snaith, *Energy Environ. Sci.* **2020**, *13*, 1776.
[46] D. P. Mcmeekin, Z. Wang, W. Rehman, F. Pulvirenti, J B. Patel, N. K. Noel, M. B. Johnston, S. R. Marder, L. M. Herz, H. J. Snaith, *Adv. Mater.* **2017**, *29*, 1607039.
[47] N. K. Noel, M. Congiu, A. J. Ramadan, S. Fearn, D. P. Mcmeekin, J. B. Patel, M. B. Johnston, B. Wenger, H. J. Snaith, *Joule* **2017**, *1*, 328.
[48] K. Yan, M. Long, T. Zhang, Z. Wei, H. Chen, S. Yang, J. Xu, *J. Am. Chem. Soc.* **2015**, *137*, 4460.
[49] N. S. Dutta, N. K. Noel, C. B. Arnold, *J. Phys. Chem. Lett.* **2020**, *11*, 5980.
[50] M. Daub, R. Stroh, H. Hillebrecht, *Chem* **2016**, *642*, 268.
[51] A. Abragam, B. Bleaney, *Electron Paramagnetic Resonance*, Clarendon Press, Oxford **1970**.
[52] M. Mekata, H. Kuriyama, Y. Ajiro, S. Mitsuda, H. Yoshizawa, *J. Magn. Magn. Mater.* **1992**, *104-107*, 859.
[53] G. van der Laan, A. I. Figueroa, *Coord. Chem. Rev.* **2014**, *95*, 277.
[54] G. van Der Laan, B. T. Thole, *Phys. Rev. B* **1991**, *43*, 13401.
[55] Y. Wang, H.-Y. Wang, M. Yu, L.-M. Fu, Y. Qin, J.-P. Zhang, X.-C. Ai, *Phys. Chem. Chem. Phys.* **2105**, *17*, 29501.

